Improved Measurement of the Evolution of the Reactor Antineutrino Flux and Spectrum at Daya Bay

F. P. An, ¹ W. D. Bai, ¹ A. B. Balantekin, ² M. Bishai, ³ S. Blyth, ⁴ G. F. Cao, ⁵ J. Cao, ⁵ J. F. Chang, ⁵ Y. Chang, ⁶ H. S. Chen, ⁵ H. Y. Chen, ⁷ S. M. Chen, ⁷ Y. Chen, ^{8,1} Y. X. Chen, ⁹ J. Cheng, ⁹ J. Cheng, ⁹ Y.-C. Cheng, ⁴ Z. K. Cheng, ¹ J. J. Cherwinka, ² M. C. Chu, ¹⁰ J. P. Cummings, ¹¹ O. Dalager, ¹² F. S. Deng, ¹³ Y. Y. Ding, ⁵ M. V. Diwan, ³ T. Dohnal, ¹⁴ D. Dolzhikov, ¹⁵ J. Dove, ¹⁶ K. V. Dugas, ¹² H. Y. Duyang, ¹⁷ D. A. Dwyer, ¹⁸ J. P. Gallo, ¹⁹ M. Gonchar, ¹⁵ G. H. Gong, ⁷ H. Gong, ⁷ W. Q. Gu, ³ J. Y. Guo, ¹ L. Guo, ⁷ X. H. Guo, ²⁰ Y. H. Guo, ²¹ Z. Guo, ⁷ R. W. Hackenburg, ³ Y. Han, ¹ S. Hans, ^{3,*} M. He, ⁵ K. M. Heeger, ²² Y. K. Heng, ⁵ Y. K. Hor, ¹ Y. B. Hsiung, ⁴ B. Z. Hu, ⁴ J. R. Hu, ⁵ T. Hu, ⁵ Z. J. Hu, ¹ H. X. Huang, ²³ J. H. Huang, ⁵ X. T. Huang, ¹⁷ Y. B. Huang, ²⁴ P. Huber, ²⁵ D. E. Jaffe, ³ K. L. Jen, ²⁶ X. L. Ji, ⁵ X. P. Ji, ³ R. A. Johnson, ²⁷ D. Jones, ²⁸ L. Kang, ²⁹ S. H. Kettell, ³ S. Kohn, ³⁰ M. Kramer, ^{18,30} T. J. Langford, ²² J. Lee, ¹⁸ J. H. C. Lee, ³¹ R. T. Lei, ²⁹ R. Leitner, ¹⁴ J. K. C. Leung, ³¹ F. Li, ⁵ H. L. Li, ⁵ G. J. Li, ⁵ S. C. Li, ²⁵ W. D. Li, ⁵ X. N. Li, ⁵ X. Q. Li, ³² Y. F. Li, ⁵ Z. B. Li, ¹ H. Liang, ¹³ C. J. Lin, ¹⁸ G. L. Lin, ²⁶ S. J. Ling, ¹ J. M. Link, ²⁵ L. Littleberg, ³ B. R. Littlejohn, ¹⁹ J. C. Liu, ⁵ J. L. Liu, ³³ J. X. Liu, ⁵ K. T. McDonald, ³⁴ R. D. McKeown, ^{36,37} Y. Meng, ³³ J. Napolitano, ²⁸ D. Naumov, ¹⁵ E. Naumova, ¹⁵ T. M. T. Nguyen, ⁶ J. P. Ochoa-Ricoux, ¹² A. Olshevskiy, ¹⁵ J. Park, ²⁵ S. Patton, ¹⁸ J. C. Peng, ¹⁶ C. S. J. Pun, ³¹ F. Z. Qi, ⁵ M. Qi, ³⁸ X. Qian, ³ N. Raper, ¹ J. Ren, ²³ C. Morales Reveco, ¹² R. Rosero, ³ B. Roskovec, ¹⁴ X. C. Ruan, ²³ B. Russell, ¹⁸ H. Steiner, ^{30,18} J. L. Sun, ³⁰ T. Tmej, ¹⁴ K. Treskov, ⁵ W. H. Tse, ¹⁰ C. E. Tull, ¹⁸ Y. C. Tung, ⁴ B. Viren, ³ V. Vorobel, ¹⁴ C. H. Wang, ⁵

(Daya Bay Collaboration)

¹Sun Yat-Sen (Zhongshan) University, Guangzhou ²University of Wisconsin, Madison, Wisconsin 53706 ³Brookhaven National Laboratory, Upton, New York 11973 ⁴Department of Physics, National Taiwan University, Taipei ⁵Institute of High Energy Physics, Beijing ⁶National United University, Miao-Li Department of Engineering Physics, Tsinghua University, Beijing ⁸Shenzhen University, Shenzhen ⁹North China Electric Power University, Beijing ¹⁰Chinese University of Hong Kong, Hong Kong ¹¹Siena College, Loudonville, New York 12211 ¹²Department of Physics and Astronomy, University of California, Irvine, California 92697 ¹³University of Science and Technology of China, Hefei ¹⁴Charles University, Faculty of Mathematics and Physics, Prague ¹⁵Joint Institute for Nuclear Research, Dubna, Moscow Region ¹⁶Department of Physics, University of Illinois at Urbana-Champaign, Urbana, Illinois 61801 ¹⁷Shandong University, Jinan ¹⁸Lawrence Berkeley National Laboratory, Berkeley, California 94720 ¹⁹Department of Physics, Illinois Institute of Technology, Chicago, Illinois 60616 ²⁰Beijing Normal University, Beijing ²¹Department of Nuclear Science and Technology, School of Energy and Power Engineering, Xi'an Jiaotong University, Xi'an ²²Wright Laboratory and Department of Physics, Yale University, New Haven, Connecticut 06520 ²³China Institute of Atomic Energy, Beijing ²⁴Guangxi University, No. 100 Daxue East Road, Nanning

²⁵Center for Neutrino Physics, Virginia Tech, Blacksburg, Virginia 24061 ²⁶Institute of Physics, National Chiao-Tung University, Hsinchu ²⁷Department of Physics, University of Cincinnati, Cincinnati, Ohio 45221 ²⁸Department of Physics, College of Science and Technology, Temple University, Philadelphia, Pennsylvania 19122 ²⁹Dongguan University of Technology, Dongguan ³⁰Department of Physics, University of California, Berkeley, California 94720 ³¹Department of Physics, The University of Hong Kong, Pokfulam, Hong Kong ³²School of Physics, Nankai University, Tianjin ³³Department of Physics and Astronomy, Shanghai Jiao Tong University, Shanghai Laboratory for Particle Physics and Cosmology, Shanghai ³⁴Joseph Henry Laboratories, Princeton University, Princeton, New Jersey 08544 35 The Hong Kong University of Science and Technology, Clear Water Bay, Hong Kong California Institute of Technology, Pasadena, California 91125 ³⁷College of William and Mary, Williamsburg, Virginia 23187 ³⁸Nanjing University, Nanjing ³⁹China General Nuclear Power Group, Shenzhen ⁴⁰College of Electronic Science and Engineering, National University of Defense Technology, Changsha ⁴¹Iowa State University, Ames, Iowa 50011 ⁴²Chongqing University, Chongqing

(Received 3 October 2022; revised 10 February 2023; accepted 27 April 2023; published 22 May 2023)

Reactor neutrino experiments play a crucial role in advancing our knowledge of neutrinos. In this Letter, the evolution of the flux and spectrum as a function of the reactor isotopic content is reported in terms of the inverse-beta-decay yield at Daya Bay with 1958 days of data and improved systematic uncertainties. These measurements are compared with two signature model predictions: the Huber-Mueller model based on the conversion method and the SM2018 model based on the summation method. The measured average flux and spectrum, as well as the flux evolution with the ²³⁹Pu isotopic fraction, are inconsistent with the predictions of the Huber-Mueller model. In contrast, the SM2018 model is shown to agree with the average flux and its evolution but fails to describe the energy spectrum. Altering the predicted inverse-beta-decay spectrum from ²³⁹Pu fission does not improve the agreement with the measurement for either model. The models can be brought into better agreement with the measurements if either the predicted spectrum due to ²³⁵U fission is changed or the predicted ²³⁵U, ²³⁸U, ²³⁹Pu, and ²⁴¹Pu spectra are changed in equal measure.

DOI: 10.1103/PhysRevLett.130.211801

The detection of reactor electron antineutrinos with the inverse-beta-decay (IBD) process plays a crucial role in advancing our knowledge of neutrinos [1–3]. Looking forward, an accurate reactor neutrino spectrum knowledge is required for the JUNO to determine the neutrino mass ordering [4,5] and for the nonproliferation goals of WATCHMAN [6].

For commercial reactors, uranium isotopes are introduced at beginning of a fueling cycle and plutonium isotopes are gradually generated. Four fission isotopes —²³⁵U, ²³⁸U, ²³⁹Pu, and ²⁴¹Pu—account for over 99.7% of the antineutrino flux with energy above the IBD

Published by the American Physical Society under the terms of the Creative Commons Attribution 4.0 International license. Further distribution of this work must maintain attribution to the author(s) and the published article's title, journal citation, and DOI. Funded by SCOAP³. detection threshold [7]. A reactor antineutrino prediction, the Huber-Mueller (HM) model [8,9], is determined by converting cumulative beta spectra to antineutrino spectra for ²³⁵U, ²³⁹Pu, and ²⁴¹Pu and by summing all involved beta decay branches in databases for ²³⁸U. The average of reactor neutrino flux measurements is only 95%–96% of the HM prediction, known as the reactor antineutrino anomaly (RAA) [10–13]. Another anomaly is with respect to the spectrum shape. The measured neutrino spectrum is poorly described by the HM model, e.g., a notable bump around 5 MeV [14–16].

The RAA and other experimental anomalies at short baseline [17–20] have motivated a new generation of short-baseline reactor neutrino experiments to search for sterile neutrinos [21–27]. The effect of weak magnetism [28], neutron capture [29], fission-neutron energy [30], and database inaccuracies [31] on the prediction has been postulated. In particular, approximately 30% of the antineutrino flux comes from forbidden decays which can

imply an uncertainty as large as the total flux deficit and the bump [32–36].

Another prediction approach, the summation method, adds up all related decay branches from databases for all four isotopes. One such example, the SM2018 calculation [37], predicted a uniformly lower flux from 235 U than the HM model. Kopeikin *et al.* [38] reported the measured ratio between cumulative β spectra from 235 U and 239 Pu that is also systematically lower than the HM prediction. Both SM2018 and Kopeikin imply a much smaller discrepancy with neutrino flux measurement than HM.

In this Letter, using the 1958-day data sample taken from December 2011 to August 2017 with the Daya Bay experiment [39], we report the measurement of the total IBD yield, σ , i.e., the number of antineutrinos per fission multiplied by the IBD cross section, and energy differential IBD yields, σ^e , i.e., the IBD yield in each energy region, and their evolution with reactor status with improved systematic uncertainties. Compared to the unfolded spectra of ²³⁵U and ²³⁹Pu [40], the measurements in this work do not introduce extra uncertainties from the unfolding method and the theoretical uncertainty of ²³⁸U and ²⁴¹Pu, which allows a more powerful examination of the combined reactor flux and spectrum prediction of the HM and SM2018 models. Other early evolution results can be found for the Daya Bay [41], NEOS [42], and RENO [43] experiments. Absolute ²³⁵U IBD yield measurement can also be found for the STEREO experiment [44].

The Daya Bay experiment, equipped with eight antineutrino detectors (ADs), measures the electron antineutrinos from six commercial reactors [39,45,46]. The IBD candidates, $\bar{\nu}_e + p \rightarrow e^+ + n$, with neutron capture on gadolinium are selected as in Ref. [39]. Approximately 3.5×10^6 IBD candidates are detected with the four nearsite ADs. The energy deposit of the positron, E_p , is related to the antineutrino energy $E_{\nu} \approx E_p + 0.78$ MeV and is reconstructed as $E_{\rm rec}$. The resolution of $E_{\rm rec}$ is about 8% at 1 MeV. A detector response matrix $M(E_{\rm rec}, E_{\nu})$ is constructed taking into account all detector effects [39]. The measured energy spectrum is corrected for the spent-nuclear-fuel contribution and the nonequilibrium contribution [40,41] for each AD and week, instead of being treated as time independent in the previous analysis [41].

The IBD yield measurement is done first. Because of the multiple reactors and detectors feature and each reactor being at a different point of its fuel cycle, a quantity N_i^{dw} is calculated for the dth AD and wth week, and i is 5, 8, 9, and 1 for 235 U, 238 U, 239 Pu, and 241 Pu, respectively [7]. It describes the number of fissions of an isotope sampled by an AD, and the definition is

$$N_i^{dw} = \sum_{r=1}^{6 \text{ reactors}} \frac{N_d^{\text{Proton}} \bar{P}_{drw}^{\text{sur}} \varepsilon}{4\pi L_{dr}^2} \frac{W_{rw} T_{dw}}{\sum_i f_{irw} e_i} f_{irw}, \qquad (1)$$

where $N_d^{\rm Proton}$ is the number of target protons of that AD, $\bar{P}_{dwr}^{\rm sur}$ is the average survival probability of reactor electron antineutrinos integrated over energy from the rth reactor to the dth AD calculated under 3-active-neutrino framework in the wth week, ε is the detection efficiency, L_{dr} is the distance of the AD-reactor pair, W_{rw} is the thermal power of the rth reactor for the wth week, which is provided by the reactor company, T_{dw} is the running time of that AD in that week, f_{irw} is the fission fraction of the ith isotope in the rth reactor and ith week, and ith isotope in the ith isotope [47]. The effective fission fraction for the ith isotope, ith isotope in the ith isotope, ith isotope in the it

Data are sorted into 13 groups according to their effective ^{239}Pu fission fraction F_9^{dw} , which represents the burnup status of reactors and is analogous to the use of F_5^{dw} [41]. In this dataset, F_9 (F_5) ranges from 0.22 to 0.36 (0.66 to 0.49). The first group corresponds to F_9 between 0.22 and 0.24, due to low statistics, with the additional 12 groups each having a 0.01 interval in F_9 from 0.24 to 0.36. The effective fission fraction of the gth group, F_i^g , is calculated as $F_i^g = \sum_{d,w \in g} N_i^{dw} / \sum_{d,w \in g} N^{dw}$, where the information in each AD and week are added together if their F_9^{dw} s belong the gth group. The effective fission fractions averaged over all detectors and time (\bar{F}_5 , \bar{F}_8 , \bar{F}_9 , and \bar{F}_1) are (0.564, 0.076, 0.304, and 0.056).

The energy differential IBD yield is measured for six reconstructed energy regions: 0.7–2, 2–3, 3–4, 4–5, 5–6, and 6–8 MeV and the energy differential yield, σ^{eg} , for the *e*th energy region and the *g*th fission group is calculated as [7,41]

$$\sigma^{eg} = \int_{e} \sum_{d,w \in g} S^{dw}(E_{\text{rec}}) dE_{\text{rec}} / \sum_{d,w \in g} N^{dwe}, \qquad (2)$$

where the integral is over the energy region, $S^{dw}(E_{\rm rec})$ is the measured energy spectrum of the dth AD in the wth week, the divisor gives the total number of fissions for the energy region, and the calculation of N^{dwe} is the same as for N^{dw} except that the neutrino survival probability in Eq. (1) is calculated for the eth $E_{\rm rec}$ region only. The sum over e is the total yield, $\sigma^g = \sum_e \sigma^{eg}$, of that group. The evolution of total and energy differential yield with F_9^g are plotted in Fig. 1.

The uncertainties in σ^g have statistical, background, and the following systematic components. For the IBD detection efficiency, the AD-correlated uncertainty is improved from 1.7% to 0.75% [11], and the AD-uncorrelated uncertainty is 0.11% [40]. The uncertainty of N_d^{Proton} is 0.92% and is AD-correlated [7]. The reactor power measurement uncertainty is 0.5% and is assigned to be reactor-uncorrelated and time-correlated [7]. The uncertainty of the energy per fission is taken into account [47].

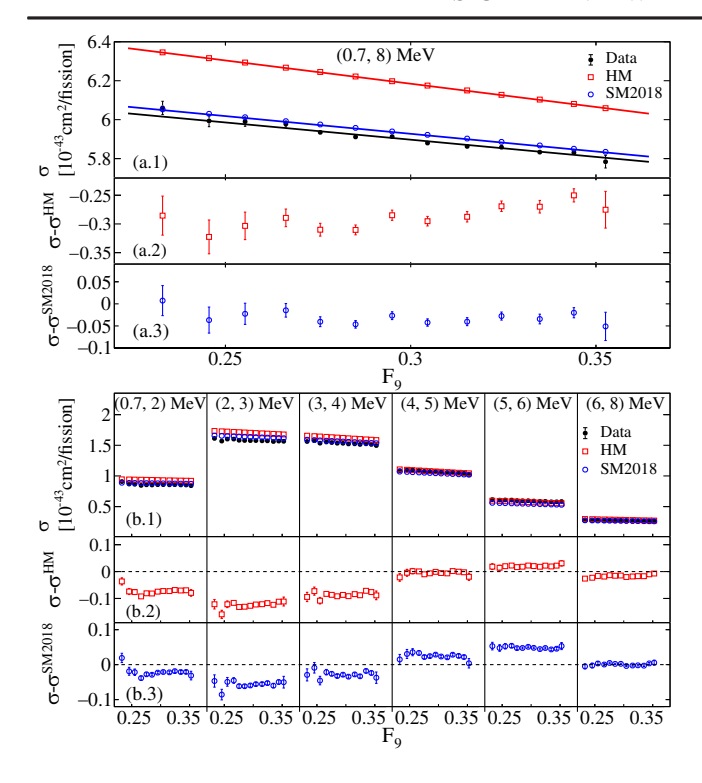


FIG. 1. Panel (a.1) shows the measured and predicted total IBD yield evolution with the effective fission fraction of 239 Pu, F_9 , and panels (a.2) and (a.3) show the measurement and prediction differences. The best-fit and best-determined lines for the measurements and predictions of the evolution are shown in (a.1). Panels (b.1), (b.2), and (b.3) show the corresponding plots for the energy differential yield evolution in six reconstructed energy regions. The units of all panels are 10^{-43} cm²/fission.

The fission fraction uncertainty for each isotope and reactor is 5%, but the uncertainties of the four isotopes are further constrained with the normalization condition and the correlation matrix [7] and are assigned to be reactorand time-correlated. The spent nuclear fuel uncertainty is improved from 100% to 30% [39]. The nonequilibrium effect uncertainty is 30% [7]. The θ_{13} -induced oscillation uncertainty is insignificant [39]. The uncertainty of the energy differential yield of σ^{eg} further includes all the energy spectrum uncertainties from the background shape and detector response [40], in which the uncertainties in the absolute energy scale are reduced to be less than 0.5% for $E_{\rm rec}$ larger than 2 MeV.

To compare with the measurement, the predicted total and energy differential yields of the *i*th isotope, $(\sigma_5, \sigma_9, \sigma_1, \sigma_8)$ and $(\sigma_5^e, \sigma_9^e, \sigma_1^e, \sigma_8^e)$ are obtained by convolving the product of model prediction and IBD cross section [7] with the detector response matrix. The total yield predictions are defined as

$$\sigma^{\text{Pred},g} \equiv F_5^g \sigma_5 + F_8^g \sigma_8 + F_9^g \sigma_9 + F_1^g \sigma_1, \tag{3}$$

where σ_i are the yields per isotope. Likewise, using the model energy differential predictions, σ_i^e , the predicted energy differential yields are

$$\sigma^{\text{Pred},eg} \equiv F_5^g \sigma_5^e + F_8^g \sigma_8^e + F_9^g \sigma_9^e + F_1^g \sigma_1^e. \tag{4}$$

The evolution plots of $\sigma^{\operatorname{Pred},g}$ and $\sigma^{\operatorname{Pred},eg}$ with F_9^g are shown in Fig. 1, as well as the differences between the measurement and predictions. The two models predict roughly the same shape but not normalization. If compared with data, deficits (bumps) can be seen around 3 MeV (5 MeV).

The uncertainties of $\sigma^{\text{Pred},g}$ and $\sigma^{\text{Pred},eg}$ are from all sources involved in the effective fission fraction calculation as described in Eqs. (1), (3), and (4). Model uncertainties are poorly defined and not included unless explicitly stated otherwise.

To understand the difference between data and predictions, the total yield evolution is compared to the predictions with two characteristic variables: average yield $\bar{\sigma}$ and normalized evolution slope $(d\sigma/dF_9)/\bar{\sigma}$. The average yield of $\bar{\sigma}$ and slope of $d\sigma/dF_9$ are two direct observables. The evolution of the predicted yield can be described as a linear function of F_9 for the observed range of F_9 . In addition, if the prediction in Eq. (3) is off by a normalization factor η , for example, induced by large-mass sterile neutrinos [10,48,49] or by a global uncertainty, e.g., from the detection efficiency, the prediction would be

$$\sigma^{\text{PredN},g} = \eta (F_5^g \sigma_5 + F_8^g \sigma_8 + F_9^g \sigma_9 + F_1^g \sigma_1). \tag{5}$$

The comparison in the normalized evolution slope $(d\sigma/dF_9)/\bar{\sigma}$ is free of any normalization issue.

The total yield measurements in the 13 fission groups are fitted to the following linear function:

$$\sigma^{\text{Lin},g} = \bar{\sigma}\{1 + [(d\sigma/dF_0)/\bar{\sigma}](F_0^g - \bar{F}_0)\},\tag{6}$$

with the χ^2 function,

$$\chi^2 = \sum_{gg'} (\sigma^g - \sigma^{\text{Lin},g}) (V^{-1})^{gg'} (\sigma^{g'} - \sigma^{\text{Lin},g}), \qquad (7)$$

to extract $\bar{\sigma}$ and $(d\sigma/dF_9)/\bar{\sigma}$, where V is a 13×13 covariance matrix determined by randomly sampling all the related uncertainty sources described above. The best-fit results are $\bar{\sigma}=(5.89\pm0.07)\times10^{-43}~{\rm cm^2/fission}$ and $[(d\sigma/dF_9)/\bar{\sigma}]=-0.300\pm0.024$ with the χ^2 over the number of degrees of freedom (NDF), $\chi^2/{\rm NDF}$, of 9.6/11. The dominant uncertainty of $\bar{\sigma}$ is from the IBD detection efficiency and number of target protons. The dominant uncertainty of $(d\sigma/dF_9)/\bar{\sigma}$ is from statistics. The uncertainties from the effective fission fraction calculation are not significant for them. The best-fit line is shown in Fig. 1, and the results and 68% confidence level contour are shown in Fig. 2.

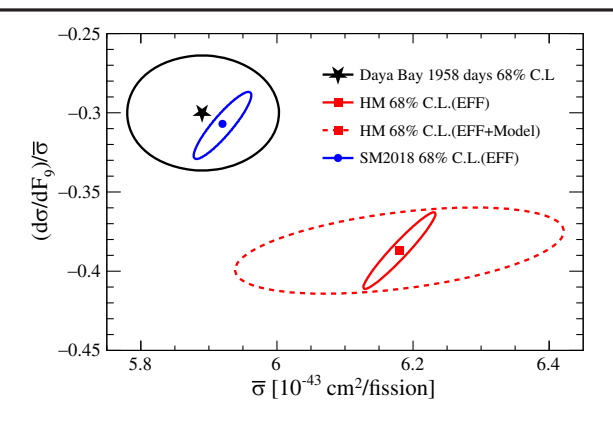


FIG. 2. The measured $\bar{\sigma}$ and $(d\sigma/dF_9)/\bar{\sigma}$ and their 68% confidence level (C.L.) contour is shown. The predictions of the HM and SM2018 models are shown with their 68% C.L. contours with effective fission fraction (EFF) uncertainty. The HM model 68% C.L. contour including its model uncertainties [8,9] is also shown.

For predictions, $\bar{\sigma}^{\rm Pred}$ and $[(d\sigma/dF_9)/\bar{\sigma}]^{\rm Pred}$ are calculated with the given $(F_5^g, F_8^g, F_9^g, F_1^g)$. The results for the HM are $\bar{\sigma}^{\rm HM} = (6.18 \pm 0.04) \times 10^{-43} \, {\rm cm}^2/{\rm fission}$ and $[(d\sigma/dF_9)/\bar{\sigma}]^{\rm HM} = -0.387 \pm 0.016 \, [(6.18 \pm 0.16) \times 10^{-43} \, {\rm cm}^2/{\rm fission}$ and -0.387 ± 0.018 if including the model uncertainties [8,9]]. The HM predictions in $\bar{\sigma}$ and $(d\sigma/dF_9)/\bar{\sigma}$ are rejected at 3.6 and 3.0 standard deviations. For SM2018, the results are consistent with the Daya Bay measurements. These results are shown in Fig. 2 and the best-determined lines are plotted in Fig. 1.

The RAA is relieved by SM2018, but the spectrum difference with data is not. The energy differential yield evolution is compared to models with the average yields and normalized evolution slopes in six reconstructed energy regions. The data are simultaneously fitted to six linear functions:

$$\sigma^{\text{Lin},eg} = \bar{\sigma}^e \{ 1 + [(d\sigma/dF_9)/\bar{\sigma}]^e (F_9^g - \bar{F}_9) \}, \quad (8)$$

with the χ^2 function,

$$\chi^2 = \sum_{eqe'q'} (\sigma^{eg} - \sigma^{\mathrm{Lin},eg}) (U^{-1})^{ege'g'} (\sigma^{e'g'} - \sigma^{\mathrm{Lin},e'g'}), \qquad (9)$$

to extract six pairs of parameters of $\bar{\sigma}^e$ and $[(d\sigma/dF_9)/\bar{\sigma}]^e$, where U is a 78 × 78 covariance matrix with a combined row (column) index of eg (e'g') for the eth (e'th) reconstructed energy region and gth (g'th) fission fraction group. U is also determined by a random sampling method of all the related uncertainty sources described earlier. The best-fit χ^2/NDF is 76/66. The six $\bar{\sigma}^e$ results are strongly correlated because their dominant uncertainties are from the IBD detection efficiency and number of target protons. The six $[(d\sigma/dF_9)/\bar{\sigma}]^e$ results are all limited by data statistics and largely uncorrelated. The correlation between

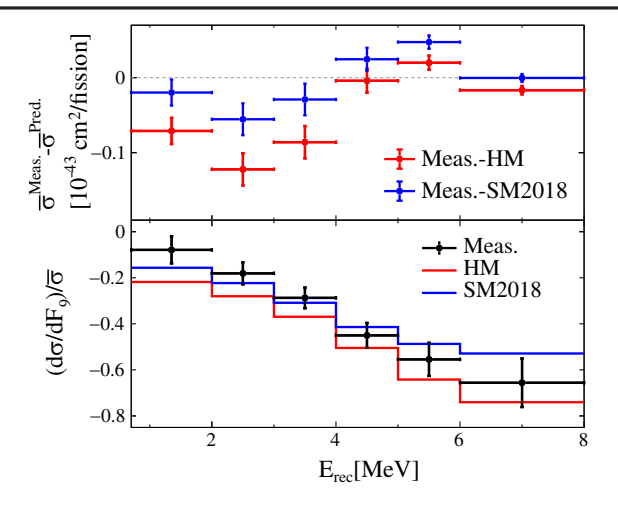


FIG. 3. The upper panel shows the difference between the measured energy differential yields and predictions for six reconstructed energy bins, where the error bars are from the measurement. The lower panel shows the normalized evolution slopes for the measurement and predictions, where the uncertainties of measurement are shown.

 $\bar{\sigma}^e$ and $[(d\sigma/dF_9)/\bar{\sigma}]^e$ is insignificant. The HM and SM2018 predictions $\bar{\sigma}^{\mathrm{Pred},e}$ and $[(d\sigma/dF_9)/\bar{\sigma}]^{\mathrm{Pred},e}$ are determined in similar manner as for the total yield study. The predictions and measurements are shown in Fig. 3. The uncertainty associated with prediction is much smaller than that from measurement.

The difference of the average IBD yields of six energy regions, $\bar{\sigma}^e$ - $\bar{\sigma}^{\mathrm{Pred},e}$, is quantified as a χ^2 with the corresponding covariance matrix. The resulting χ^2/NDF and the corresponding rejection level in standard deviations are shown in Table I. The models do not agree with Daya Bay, and because of the deficit around 3 MeV and/or the bump around 5 MeV found in the measurement and the strong correlation among the measurements in the six energy regions, their χ^2/NDF s are rather large, reaching 25 and 27 standard deviations for the HM and SM2018 models, respectively.

The normalized evolution slopes of the six energy regions, $[(d\sigma/dF_9)/\bar{\sigma}]^e$, are compared to HM and SM2018. Their difference is quantified with a χ^2 calculated with the corresponding covariance matrix. The resulting χ^2/NDF is shown in Table I. While the HM and SM2018 models poorly predict the spectral shape, their predicted relative changes with the fuel composition have much better agreement with the measurement.

To understand these flux and/or shape differences, three types of modified models with new free parameters are introduced on top of the HM and SM2018 predictions.

The first modification to each model is to alter only the ²³⁵U energy differential yield prediction in each reconstructed energy region by the fraction f_5^e together with the global normalization factor η , as in Eq. (5):

TABLE I. Comparison results of the measurement with the HM and SM2018 predictions for the energy differential IBD yield evolution. Columns 2 and 3 show the χ^2/NDF and N_σ (rejection level in standard deviations) for the average IBD yields of six energy regions, $\bar{\sigma}^e$, comparison and columns 4 and 5 show the χ^2/NDF and N_σ for the normalized evolution slopes, $[(d\sigma/dF_9)/\bar{\sigma}]^e$, comparison.

	$ar{\sigma}^e$	$ar{\sigma}^e$		$[(d\sigma/dF_9)/\bar{\sigma}]^e$		
Model	χ^2/NDF	N_{σ}	χ^2/NDF	N_{σ}		
HM SM2018	675/6 748/6	25σ 27σ	11/6 5.5/6	1.8σ 0.7σ		

$$\sigma^{\text{model},eg} = \eta [F_5^g \sigma_5^e (1 + f_5^e) + F_8^g \sigma_8^e + F_9^g \sigma_9^e + F_1^g \sigma_1^e]. \quad (10)$$

Depending on the base model, the modified models are further labeled as $\rm HM + ^{235}U$ and $\rm SM2018 + ^{235}U$. This is motivated by the fact that the majority of the neutrino flux is due to ^{235}U .

In the second modification to each model, the prediction is

$$\sigma^{\text{model},eg} = \eta [F_5^g \sigma_5^e + F_8^g \sigma_8^e + F_9^g \sigma_9^e (1 + f_9^e) + F_1^g \sigma_1^e], \quad (11)$$

where only the 239 Pu energy differential yield predictions in each reconstructed energy region are allowed to change by the fraction f_9^e together with the global normalization factor η . The modified models are labeled as HM + 239 Pu and SM2018 + 239 Pu next. This is motivated given that 239 Pu is the second largest contributor to the neutrino flux.

The third modification to each model is to equally scale the predicted spectra of four isotopes in each reconstructed energy region by the fraction f_E^e :

$$\sigma^{\text{model},eg} = (1 + f_{\text{E}}^e)[F_5^g \sigma_5^e + F_8^g \sigma_8^e + F_9^g \sigma_9^e + F_1^g \sigma_1^e]. \quad (12)$$

The motivation is that particular studies [33,50] have suggested that all four isotopes may have a common problem in predictions. They are labeled as HM + Equ and SM2018 + Equ.

We fit the measured energy differential yields evolution to the modified models with free parameters of six f_e s and/ or η using the following χ^2 :

$$\chi^{2} = \sum_{ege'g'} (\sigma^{eg} - \sigma^{\text{model},eg}) (Q^{-1})^{ege'g'} (\sigma^{e'g'} - \sigma^{\text{model},e'g'}),$$

$$\tag{13}$$

where Q is a 78×78 covariance matrix including all uncertainties for the measurement and predictions determined as V of Eq. (7) or U of Eq. (9). When testing Eq. (10) or Eq. (11), fits are also performed with η fixed to 1.

TABLE II. For the six modified models in Eqs. (10)–(12), the best-fit normalization factor η , χ^2/NDF , and N_σ (rejection level in standard deviations) are shown in columns 2, 3, and 4. Columns 5 and 6 are for the χ^2/NDF and N_σ when fitting with η fixed to 1.

				χ^2/NDF	N_{σ}
Model	η	χ^2/NDF	N_{σ}	$(\eta = 1)$	$(\eta = 1)$
$HM + {}^{235}U$	0.985 ± 0.021	83/71	1.4σ	83/72	1.4σ
$SM2018 + {}^{235}U$	0.997 ± 0.021	80/71	1.2σ	80/72	1.2σ
$HM + {}^{239}Pu$	0.935 ± 0.014	116/71	3.4σ	136/72	4.5σ
$SM2018 + {}^{239}Pu$	0.995 ± 0.014	126/71	4.0σ	127/72	4.0σ
HM + Equ	NA	89/72	1.7σ	NA	NA
SM2018 + Equ	NA	82/72	1.3σ	NA	NA

The best-fit χ^2/NDF , the corresponding rejection level in standard deviations, and best-fit η , when applicable, are shown in Table II. The best-fit f_5^e and f_9^e of Eqs. (10) and (11) with η fixed to 1, and f_E^e in Eq. (12) are shown in the upper panels of Fig. 4. The difference of the deduced $\bar{\sigma}^{\text{model},e}$ with measurement and the deduced

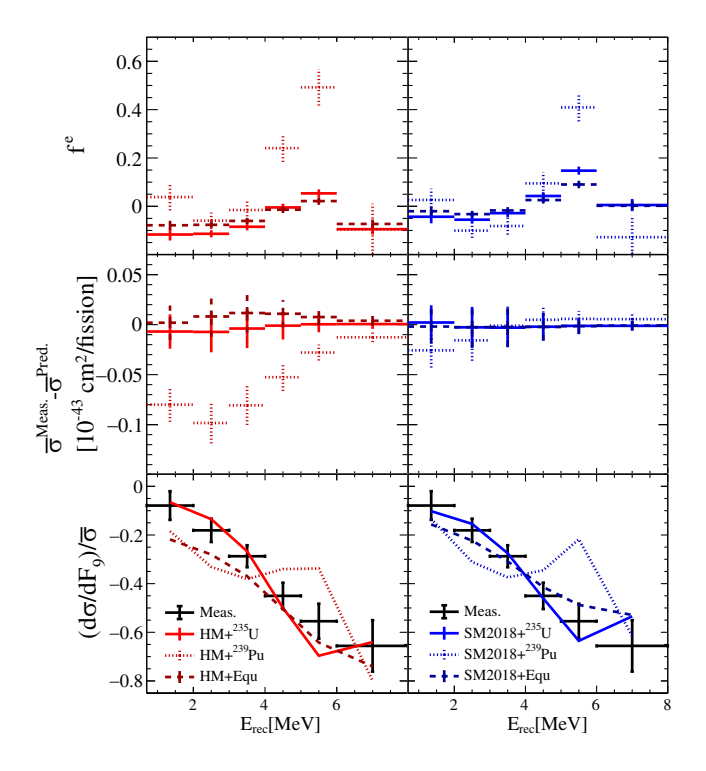


FIG. 4. The best-fit f^e , i.e., f_5^e , f_9^e , or f_E^e , of the modified models of HM + 235 U, SM2018 + 235 U [Eq. (10) with η fixed to 1], HM + 239 Pu, SM2018 + 239 Pu [Eq. (11) with η fixed to 1], HM + Equ, and SM2018 + Equ [Eq. (12)] are shown in the upper panels, where the error bars are fit results. The deduced $\bar{\sigma}^{\text{model},e}$ predictions with the corresponding f^e values for each model are shown as the difference with the measurement in the middle panels and the error bars shown are from the measurement. The measured $[(d\sigma/dF_9)/\bar{\sigma}]^e$ and deduced $[(d\sigma/dF_9)/\bar{\sigma}]^{\text{model},e}$ are shown in the lower panels and the error bars shown are from the measurement.

 $[(d\sigma/dF_9)/\bar{\sigma}]^{\text{model},e}$ are also shown in the middle and lower panels of Fig. 4, respectively, where the first and third model modifications are preferred with respect to the second model.

Even when the 239 Pu energy spectra are modified, both the HM and SM2018 model predictions remain incompatible with the data at well over 3 standard deviations as shown in Table II. For both models, as seen in Fig. 4, the required changes of the 239 Pu spectrum in some regions are higher than 40%, which is beyond the range of uncertainties by the various postulated mechanisms [28–36] and is unreasonable. This observation can be phenomenologically traced back to the features of Fig. 1. For example, the $\bar{\sigma}^e$ - $\bar{\sigma}^{HM,e}$ in the 2–4 MeV region shows a positive slope and is not proportional to F_9 , which contradicts the assumption of a pure 239 Pu-caused anomaly [42,43].

The attempts to adjust the predicted spectrum of ^{235}U or all spectra in equal measure all lead to good agreement with the data using this metric. As shown in Table II, their best-fit η results for ^{235}U -adjusting models are all consistent with 1. The deduced $\bar{\sigma}^{\text{model},e}$ and $[(d\sigma/dF_9)/\bar{\sigma}]^{\text{model},e}$ are consistent with the measurements as shown in Fig. 4. HM + ^{235}U works slightly better than HM + Equ model, as their best-fit χ^2/NDF shown in Table II.

In summary, the SM2018 prediction of the total IBD yield evolution is found to be more compatible with the data than the HM model. But the predictions of spectrum for both HM and SM2018 models show large discrepancies from the data. We exclude at high significance the hypothesis that the ²³⁹Pu energy spectrum in HM or SM2018 models is responsible for the entire difference with the data, regardless of how the normalization of the Daya Bay data is treated. In contrast, good consistency with the data can be achieved either by altering the ²³⁵U spectrum or all four isotopes spectra in equal measure in the SM2018 model. For the HM model, the ²³⁵U spectrum adjustment works slightly better than adjusting all spectra. Future enhancements to the models could prioritize ²³⁵Uspecific causes or factors common to the four isotopes. The key analysis information is provided in the Supplemental Material [51].

Daya Bay is supported in part by the Ministry of Science and Technology of China, the U.S. Department of Energy, the Chinese Academy of Sciences, the National Natural Science Foundation of China, the Guangdong Provincial Government, the Shenzhen municipal government, the China General Nuclear Power Group, Key Laboratory of Particle and Radiation Imaging (Tsinghua University), the Ministry of Education, Key Laboratory of Particle Physics and Particle Irradiation (Shandong University), the Ministry of Education, Shanghai Laboratory for Particle Physics and Cosmology, the Research Grants Council of the Hong Kong Special Administrative Region of China, the University Development Fund of The University of

Hong Kong, the MOE program for Research of Excellence at National Taiwan University, National Chiao-Tung University, and NSC fund support from Taiwan, the U.S. National Science Foundation, the Alfred P. Sloan Foundation, the Charles University Research Center UNCE/SCI/013 in the Czech Republic, the Joint Institute of Nuclear Research in Dubna, Russia, the CNFC-RFBR joint research program, the National Commission of Scientific and Technological Research of Chile, and the Tsinghua University Initiative Scientific Research Program. We acknowledge Yellow River Engineering Consulting Co., Ltd., and China Railway 15th Bureau Group Co., Ltd., for building the underground laboratory. We are grateful for the ongoing cooperation from the China General Nuclear Power Group and China Light and Power Company.

^{*}Present address: Department of Chemistry and Chemical Technology, Bronx Community College, Bronx, New York 10453.

[†]Present address: Department of Physics and Astronomy, University of Rochester, Rochester, New York 14627.

[‡]Present address: Department of Physics and Astronomy, Louisiana State University, Baton Rouge, Louisiana 70803.

^[1] F. Reines and C. L. Cowan, Nature (London) **178**, 446 (1956).

^[2] K. Eguchi *et al.* (KamLAND Collaboration), Phys. Rev. Lett. **90**, 021802 (2003).

^[3] F. P. An *et al.* (Daya Bay Collaboration), Phys. Rev. Lett. **108**, 171803 (2012).

^[4] F. An et al. (JUNO Collaboration), J. Phys. G 43, 030401 (2016).

^[5] A. Abusleme *et al.* (JUNO Collaboration), arXiv:2005. 08745.

^[6] M. Askins et al. (WATCHMAN Collaboration), arXiv:1502. 01132.

^[7] F. P. An et al. (Daya Bay Collaboration), Chin. Phys. C 41, 013002 (2017).

^[8] P. Huber, Phys. Rev. C 84, 024617 (2011).

^[9] T. A. Mueller et al., Phys. Rev. C 83, 054615 (2011).

^[10] G. Mention, M. Fechner, Th. Lasserre, Th. A. Mueller, D. Lhuillier, M. Cribier, and A. Letourneau, Phys. Rev. D 83, 073006 (2011).

^[11] D. Adey et al. (Daya Bay Collaboration), Phys. Rev. D 100, 052004 (2019).

^[12] S. G. Yoon *et al.* (RENO Collaboration), Phys. Rev. D **104**, L111301 (2021).

^[13] H. de Kerret *et al.* (Double Chooz Collaboration), Nat. Phys. **16**, 558 (2020).

^[14] F. P. An *et al.* (Daya Bay Collaboration), Phys. Rev. Lett. 116, 061801 (2016).

^[15] J. H. Choi *et al.* (RENO Collaboration), Phys. Rev. Lett. **116**, 211801 (2016).

^[16] Y. Abe *et al.* (Double Chooz Collaboration), J. High Energy Phys. 10 (2014) 086.

^[17] A. Aguilar-Arevalo *et al.* (LSND Collaboration), Phys. Rev. D **64**, 112007 (2001).

- [18] A. A. Aguilar-Arevalo et al. (MiniBooNE Collaboration), Phys. Rev. Lett. 105, 181801 (2010).
- [19] P. Anselmann *et al.* (GALLEX Collaboration), Phys. Lett. B 342, 440 (1995).
- [20] J. N. Abdurashitov *et al.* (SAGE Collaboration), Phys. Rev. C 80, 015807 (2009).
- [21] I. Alekseev et al., Phys. Lett. B 787, 56 (2018).
- [22] Y. J. Ko et al. (NEOS Collaboration), Phys. Rev. Lett. 118, 121802 (2017).
- [23] A. Serebrov et al. (NEUTRINO-4 Collaboration), Pis'ma Zh. Eksp. Teor. Fiz. 109, 209 (2019).
- [24] M. Andriamirado *et al.* (PROSPECT Collaboration), Phys. Rev. D **103**, 032001 (2021).
- [25] Y. Abreu *et al.* (SoLid Collaboration), J. Instrum. 14, P11003 (2019).
- [26] H. Almazán *et al.* (STEREO Collaboration), Nature (London) **613**, 257 (2023).
- [27] V. V. Barinov et al., Phys. Rev. Lett. 128, 232501 (2022).
- [28] X. B. Wang and A. C. Hayes, Phys. Rev. C 95, 064313 (2017).
- [29] P. Huber and P. Jaffke, Phys. Rev. Lett. 116, 122503 (2016).
- [30] B. R. Littlejohn, A. Conant, D. A. Dwyer, A. Erickson, I. Gustafson, and K. Hermanek, Phys. Rev. D 97, 073007 (2018).
- [31] A. C. Hayes, J. L. Friar, G. T. Garvey, D. Ibeling, G. Jungman, T. Kawano, and R. W. Mills, Phys. Rev. D 92, 033015 (2015).
- [32] A. C. Hayes, J. L. Friar, G. T. Garvey, G. Jungman, and G. Jonkmans, Phys. Rev. Lett. 112, 202501 (2014).
- [33] L. Hayen, J. Kostensalo, N. Severijns, and J. Suhonen, Phys. Rev. C 100, 054323 (2019).
- [34] Y.-F. Li and D. Zhang, Phys. Rev. D 100, 053005 (2019).
- [35] D.-L. Fang and B. A. Brown, Phys. Rev. C 91, 025503 (2015).

- [36] A. A. Sonzogni, T. D. Johnson, and E. A. McCutchan, Phys. Rev. C **91**, 011301(R) (2015).
- [37] M. Estienne et al., Phys. Rev. Lett. 123, 022502 (2019).
- [38] V. Kopeikin, M. Skorokhvatov, and O. Titov, Phys. Rev. D 104, L071301 (2021).
- [39] D. Adey et al. (Daya Bay Collaboration), Phys. Rev. Lett. 121, 241805 (2018).
- [40] D. Adey *et al.* (Daya Bay Collaboration), Phys. Rev. Lett. **123**, 111801 (2019).
- [41] F. P. An et al. (Daya Bay Collaboration), Phys. Rev. Lett. 118, 251801 (2017).
- [42] P. Huber, Phys. Rev. Lett. 118, 042502 (2017).
- [43] G. Bak et al. (RENO Collaboration), Phys. Rev. Lett. 122, 232501 (2019).
- [44] H. Almazán *et al.* (STEREO Collaboration), Phys. Rev. Lett. **125**, 201801 (2020).
- [45] F. P. An et al. (Daya Bay Collaboration), Phys. Rev. D 93, 072011 (2016).
- [46] F. An et al. (Daya Bay Collaboration), Phys. Rev. D 95, 072006 (2017).
- [47] X. B. Ma, W. L. Zhong, L. Z. Wang, Y. X. Chen, and J. Cao, Phys. Rev. C 88, 014605 (2013).
- [48] F. P. An et al. (Daya Bay Collaboration), Phys. Rev. Lett. 113, 141802 (2014).
- [49] A. Palazzo, J. High Energy Phys. 10 (2013) 172.
- [50] M. Xubo, Y. Le, Z. Liang, A. Fengpeng, and C. Jun, arXiv: 1807.09265.
- [51] See Supplemental Material at http://link.aps.org/supplemental/ 10.1103/PhysRevLett.130.211801 for the total and differential IBD yield measurements and the three covariance matrices.